Research Article | Open Access

Microstructures

Wang *et al*. *Microstructures* **2026**, *6*, 20260109 **DOI:**10.20517/microstructures.2026.40

Gradient microcellular materials for broadband microwave absorption and multifunctional integration

Xiaojia Wang[1], Yichong Chen[1,2], Ke Lei[1], Xuwei Li[1], Jiayang Sun[1], Dongdong Hu[1], Ling Zhao[1,2]

Keywords:
Gradient microcellular structure, microwave absorption, multiple functions, radar stealth

Citation: Wang, X.; Chen, Y.; Lei, K.; Li, X.; Sun, J.; Hu, D.; Zhao, L. Gradient microcellular materials for broadband microwave absorption and multifunctional integration. *Microstructures* **2026**, *6*, 20260109. https://dx.doi.org/10.20517/microstructures.2026.40

Received: 25 Mar 2026
First Decision: 9 May 2026
Revised: 21 May 2026
Accepted: 16 Jun 2026
Published: 21 Aug 2026

Academic Editors: Lei Xu, Shiqing Deng
Copy Editor: Fangling Lan
Production Editor: Fangling Lan

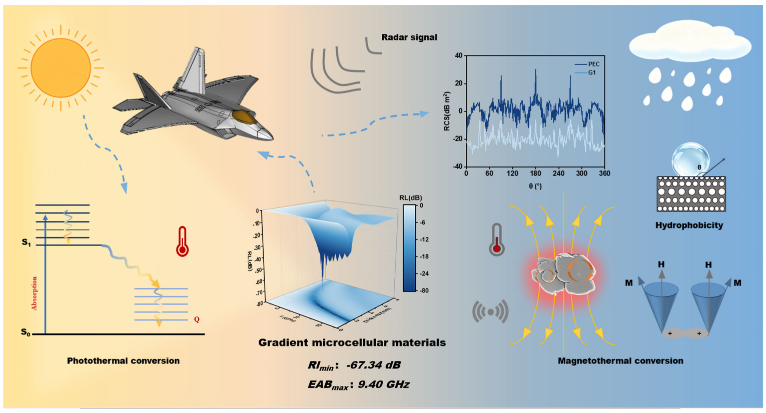

Abstract

Lightweight electromagnetic wave absorption materials with integrated multifunctionality are highly desirable for advanced civilian and military applications operating in complex environments. Herein, gradient microcellular flaky carbonyl iron powder (FCIP)/graphene (GP)/styrene-ethylene-butylene-styrene block copolymer (SEBS) materials are constructed via a one-step supercritical N_2 foaming strategy by precisely regulating foaming parameters and cell size, thereby generating a gradient microcellular architecture along the thickness direction. This singular gradient structure effectively alleviates the impedance mismatch while simultaneously enhancing electromagnetic absorption through multiple loss mechanisms, including dielectric loss, magnetic loss, and multiple reflection and scattering. As a result, the gradient microcellular FCIP/GP/SEBS materials exhibit markedly improved microwave absorption (MA) performance relative to their uniform counterpart, achieving a reflection loss of -67.34 dB at 2.21 mm and an effective absorption bandwidth of 9.40 GHz at 1.99 mm, nearly covering the entire X and Ku bands. In addition, radar cross-section simulations on a plate and an F-35 fighter model confirm the excellent

[1]State Key Laboratory of Chemical Engineering and Low-Carbon Technology, Shanghai Key Laboratory of Multiphase Materials Chemical Engineering, School of Chemical Engineering, East China University of Science and Technology, Shanghai 200237, China.
[2]Shanghai Electronic Chemicals Innovation Institute, East China University of Science and Technology, Shanghai 201419, China.

Correspondence to: Dr. Yichong Chen, Prof. Ling Zhao, State Key Laboratory of Chemical Engineering and Low-Carbon Technology, Shanghai Key Laboratory of Multiphase Materials Chemical Engineering, School of Chemical Engineering, East China University of Science and Technology, Shanghai 200237, China. E-mail: chenyc@ecust.edu.cn; zhaoling@ecust.edu.cn

radar stealth capability of the gradient microcellular materials. Besides, the materials also exhibit favorable mechanical performance, excellent hydrophobicity, and stable photothermal and magnetothermal conversion, endowing them with thermal management and multi-field-responsive functionalities. This work provides a facile and scalable strategy for designing lightweight, broadband, and multifunctional MA materials with significant application potential for stealth protection, energy conversion, and service in harsh environments.

INTRODUCTION

Electromagnetic wave (EMW) pollution and radar detection have become increasingly critical issues with the rapid development of wireless communication, high-frequency electronic devices, and modern stealth technology[1-3]. Accordingly, lightweight high-performance and broadband microwave absorption (MA) materials have attracted extensive attention in both civilian and military fields[4,5]. Excellent MA performance fundamentally depends on a delicate balance between impedance matching and EMW attenuation, while simultaneously achieving both remains challenging. Among the various design strategies, constructing gradient structures has been widely recognized as an effective approach to improving MA performance[6], because gradually varied electromagnetic parameters can simultaneously optimize impedance matching and attenuation capability[7]. To date, gradient structure have mainly been fabricated through layer-by-layer stratification[8], multi-layer freeze-drying[9]and 3D printing[10,11]. These approaches can construct spatial variations in composition[12], conductivity[13], or electromagnetic parameters[7], thereby improving impedance matching. However, the MA materials with gradient structure fabricated by the aforementioned methods still suffer from several limitations, including excessive thickness, interlayer discontinuity, and cumbersome process, making it difficult to simultaneously meet the practical requirements for high MA performance and multifunctionality[14,15]. Therefore, the fabrication of MA materials with a monolithic gradient structure and continuous spatial variation remains a significant challenge.

Recently, polymer-based microcellular materials provide a promising platform for lightweight MA materials because their low density, excellent processability, and tunable microcellular structures[7,16,17]. Supercritical fluid foaming technology provides an effective route for fabricating continuously gradient microcellular structure[18,19]. The gradient structure contributes to the optimization of impedance matching and light microcellular structure facilitates multiple reflections and scattering of EMW within the material, enhancing EMW absorption and attenuation[7,8,20-22]. Therefore, integrating gradient architectures with microcellular structures to construct gradient microcellular structure is expected to simultaneously achieve strong EMW attenuation and improved impedance matching, thereby enhancing MA and broadening the effective absorption bandwidth (EAB)[14,23]. For example, *via* supercritical carbon dioxide (scCO_2), Monnereau *et al.*[24] prepared gradient polycarbonate/carbon nanotube based nanocomposites foams exhibiting a higher shielding effectiveness with a high ability to absorb the incident radiation than homogeneous foams. Nevertheless, the current studies remain limited by difficulties in achieving continuous and controllable gradient architectures, as well as by the strong sensitivity of the foaming behavior to material composition and processing conditions[25,26]. In addition, the simultaneous realization of optimized impedance matching, strong attenuation capability, and multifunctional integration within a monolithic material system remains a considerable challenge[27-31].

Herein, we report a one-step supercritical N_2 foaming strategy for the fabrication of gradient microcellular materials. Highly anisotropic magnetic flaky carbonyl iron powder (FCIP) and highly conductive graphene (GP) were selected as dual fillers, with styrene-ethylene-butylene-styrene block copolymer (SEBS) serving as the polymer matrix, and the FCIP/GP/SEBS composites were fabricated *via* melt blending. By regulating saturation pressure, saturation temperature, and saturation time in foaming process, the integrated and controllable fabrication of a gradient microcellular structure was realized, effectively overcoming the limitations of interlayer delamination imposed by conventional gradient architectures. The synergy between the gradient microcellular structure and the magnetic-dielectric component design enabled gradient impedance matching while preserving strong EMW attenuation. Consequently, the material achieved an EAB of 9.40 GHz at a thickness of 1.99 mm and a minimum reflection loss (RL) of -67.34 dB at 2.21 mm. Beyond its excellent MA performance, the material also exhibited hydrophobicity, outstanding mechanical strength, and stable magnetothermal and photothermal conversion capabilities, highlighting its potential for diverse application scenarios.

MATERIALS AND METHODS

Materials

SEBS (S6553) was purchased from Zhejiang Zhongli Synthetic Materials Technology Co., Ltd. FCIP (TSPZ_ZH01) were provided by Tiany New Material Technology Co., Ltd. GP (NCT-APS) were obtained from Changzhou Carbon New Material Technology Co., Ltd. N_2 (99.999%) was provided by Air Production Co., Ltd.

Fabrication process

As illustrated in Figure 1A, FCIP, GP, and SEBS were melt-blended in a torque rheometer (HAAKE Polylab 557-1306, Thermo Fisher, USA), at 180 °C and 50 rpm/min for 10 min. The resulting composites were compression-molded at 180 °C into disks with a diameter of 30 mm and a thickness of 4 mm by hot press machine (TH-XC601-HC100, Xutaiheng., China). The obtained disks were then subjected to electron beam irradiation for modification at a dose of 150 kGy to prepare FCIP/GP/SEBS composites with varying GP content.

Both uniform and gradient microcellular materials were fabricated *via* supercritical N_2 foaming. The detailed procedure is as follows:

(1) Samples were placed in an autoclave, purged three times with N_2 to remove air, and then heated to the foaming temperature in an oil bath, followed by pressurization to the desired pressure using an ISCO pump (100DX, Teledyne ISCO, USA).

(2) For the fabrication of uniform microcellular materials, the N_2 saturation time was 1.0 h, whereas for the preparation of gradient microcellular materials, the N_2 saturation time was 15-120 s.

(3) Subsequently, the desired samples were obtained by rapid depressurization at 80 MPa/s.

In the FCIP/GP/SEBS composites, the FCIP content was fixed at 75 wt.%, while the GP contents were 0.5, 1.0, 1.5, and 2.0 wt.%, respectively, and were sequentially designated as N1, N2, N3, and N4. Their uniform microcellular counterparts with an expansion ratio of 2 were designated as U1, U2, U3, and U4, and the corresponding gradient microcellular materials with an expansion ratio of 2 were labeled G1, G2, G3, and G4. Detailed descriptions of the structural and performance characterizations are provided in the Supplementary Materials.

RESULTS AND DISCUSSION

Composition and structure of FCIP/GP/SEBS composites and their microcellular materials

In the material design presented herein, supercritical N_2 foaming serves as the crucial process for fabricating gradient microcellular materials. As illustrated in Figure 1A, during the incomplete saturation stage, a N_2 concentration gradient is established across the sample thickness, developing the nucleation density to

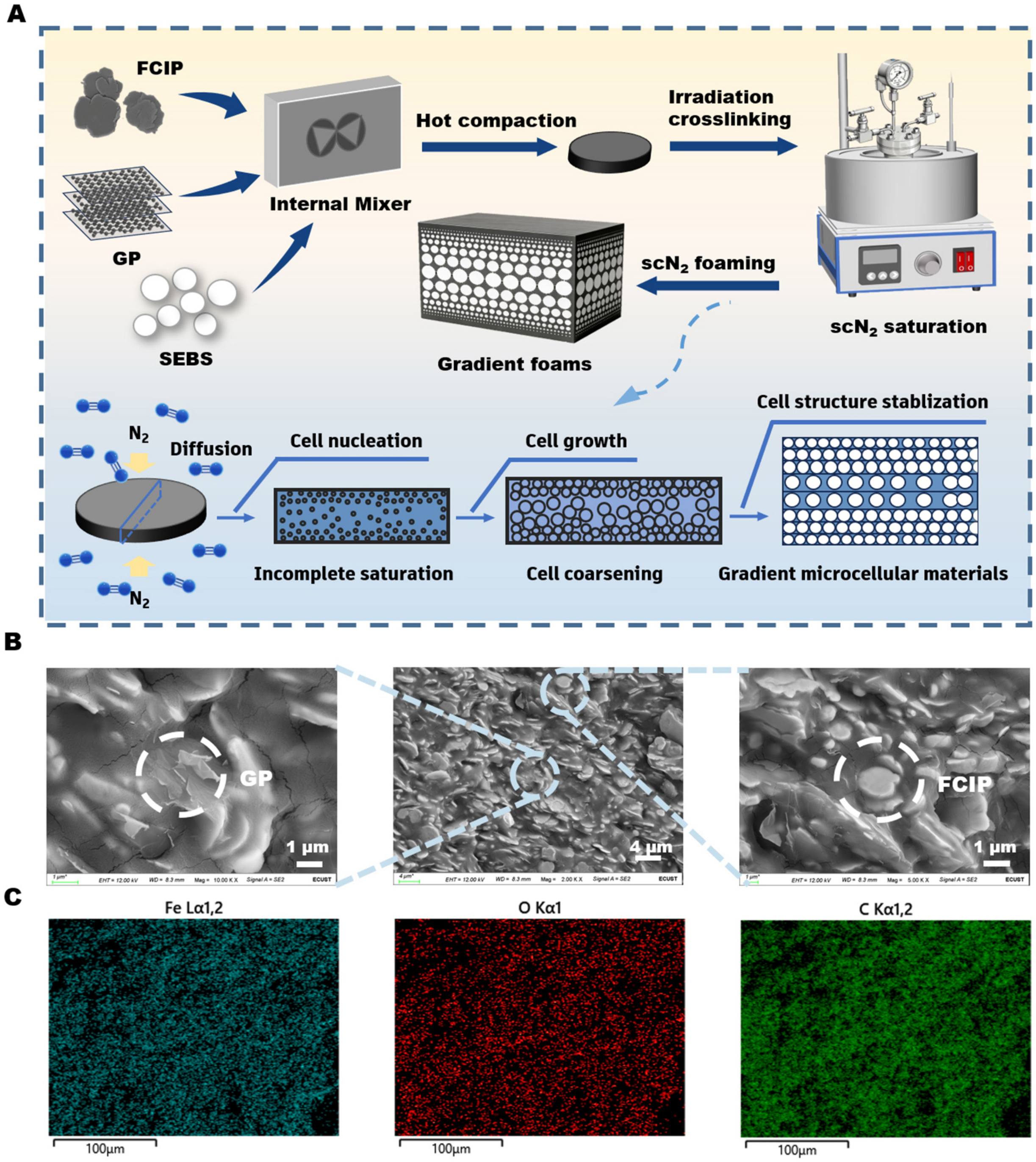

Figure 1. Fabrication Process and Composition Characterization. (A) Schematic of fabricating FCIP/GP/SEBS composite and their microcellular materials; (B) Cross-sectional morphology of FCIP/GP/SEBS composite and (C) EDS mapping of Fe, O and C elements in FCIP/GP/SEBS composite.

increase progressively from the edge to the interior. After cell growth and stabilization, a distinct gradient microcellular architecture is obtained. The incorporation of FCIP and GP as dual magnetic-dielectric fillers plays a decisive role in the EMW absorption performance of the composites[32]. As shown in Figure 1B, the fabricated FCIP/GP/SEBS composites show abundant heterogeneous interfaces, which is beneficial to EMW absorption[33]. Energy-dispersive X-ray spectroscopy (EDS) further elucidates the composition and distribution of the fillers within the composite. As shown in Figure 1C, the elemental mapping of Fe, O, and

C further evidence that the fillers are homogeneously dispersed throughout the SEBS matrix, with no apparent agglomeration.

In supercritical N_2 foaming processes, the cell morphology is governed by multiple factors, such as the blowing agent, foaming method, and processing conditions. In this study, a series of microcellular materials were fabricated using supercritical N_2 foaming technology by adjusting foaming conditions, including saturation pressure, saturation temperature, and saturation time. The addition of FCIP and GP enhanced the viscoelasticity of the composites [Supplementary Figure 1], which in turn affected the foaming behavior[34]. Detailed data are provided in the Supplementary Materials [Supplementary Figures 2 and 3, Supplementary Tables 1-3]. Based on these results, this study focuses on uniform and gradient microcellular FCIP/GP/SEBS materials with an expansion ratio of 2 to elucidate how the gradient structure affects the MA performance at varying filler contents.

Figure 2A-H shows SEM images of the gradient and uniform microcellular FCIP/GP/SEBS materials with an expansion ratio of 2, all of which exhibit similar cell structures. The corresponding cell statistics are summarized in Figure 2I-K. The uniform microcellular materials U1-U4 display relatively homogeneous distributions of cell size and cell density. In contrast, in the gradient microcellular materials G1-G4, the cell size increases from the edge to the center, while the cell density correspondingly decreases. Figure 2L presents the EDS elemental mapping of Fe, revealing a progressive increase in filler content from the edge toward the center of the gradient microcellular material. This gradient in filler distribution is attributed to the decrease in porosity from the edge to the center, as demonstrated by the three-dimensional micro-CT reconstruction images shown in Figure 2M–P. Therefore, this unique gradient structure is more conducive to EMW absorption and dissipation[7,35].

Microwave absorption performance

Minimum reflection loss (RL_{min}) and maximum effective absorption bandwidth (EAB_{max}) are two key indicators for evaluating the MA performance of FCIP/GP/SEBS materials[36]. Figure 3A-J, Supplementary Figures 4 and 5 show the MA properties of FCIP/GP/SEBS materials with the same expansion ratio of 2 but different microstructures, and the corresponding statistics are summarized in Figure 3K-N. Both the gradient and uniform microcellular materials exhibit better absorption performance than the FCIP/GP/SEBS composites, demonstrating the enhancement of microcellular structure in EMW dissipation (Figure 3A-J, Supplementary Figures 4 and 5). Owing to the singular gradient microcellular structure, G1 achieves an EAB of 9.40 GHz (8.6-18.0 GHz, nearly covering the entire X and Ku bands) at 1.99 mm and a RL of -67.34 dB at 2.21 mm which significantly exceeds that of U1 (7.70 GHz at 1.72 mm, -54.39 dB at 2.34 mm). Similarly, the gradient microcellular FCIP/GP/SEBS materials G2, G3 and G4 exhibit an EAB of 9.16 GHz at 1.77 mm, 8.95 GHz at 1.75 mm and 9.10 GHz at 1.68 mm, respectively, demonstrating superior MA performance compared with their corresponding uniform microcellular counterparts U2 (8.20 GHz at 1.69 mm), U3 (7.90 GHz at 1.70 mm), and U4 (8.09 GHz at 1.66 mm) as depicted in Figure 3K and L. Notably, G2 exhibited an exceptionally outstanding RL of -77.25 dB at a thickness of 2.44 mm. As illustrated in Figure 3M and N, the EAB of G1 is enhanced by up to 1.7 GHz relative to that of the U1 and the RL_{min} of G2 decreases by 20.56 dB relative to that of U2, underscoring the important role of the gradient microcellular structure in EMW absorption. The broadband EMW absorption capability of the gradient microcellular materials can be attributed to several synergistic factors, including improved impedance matching, which promotes greater EMW penetration into the material interior[8]; multiple reflections and scattering induced by the microcellular structure[37]; and the combined dielectric and magnetic loss effects arising from the dual FCIP and GP fillers[32,38]. Figure 3O and Supplementary Table 4 benchmark this work against representative prior absorbers. Both G1 and G2 achieve high RL and excellent EAB, demonstrating superior MA absorption performance.

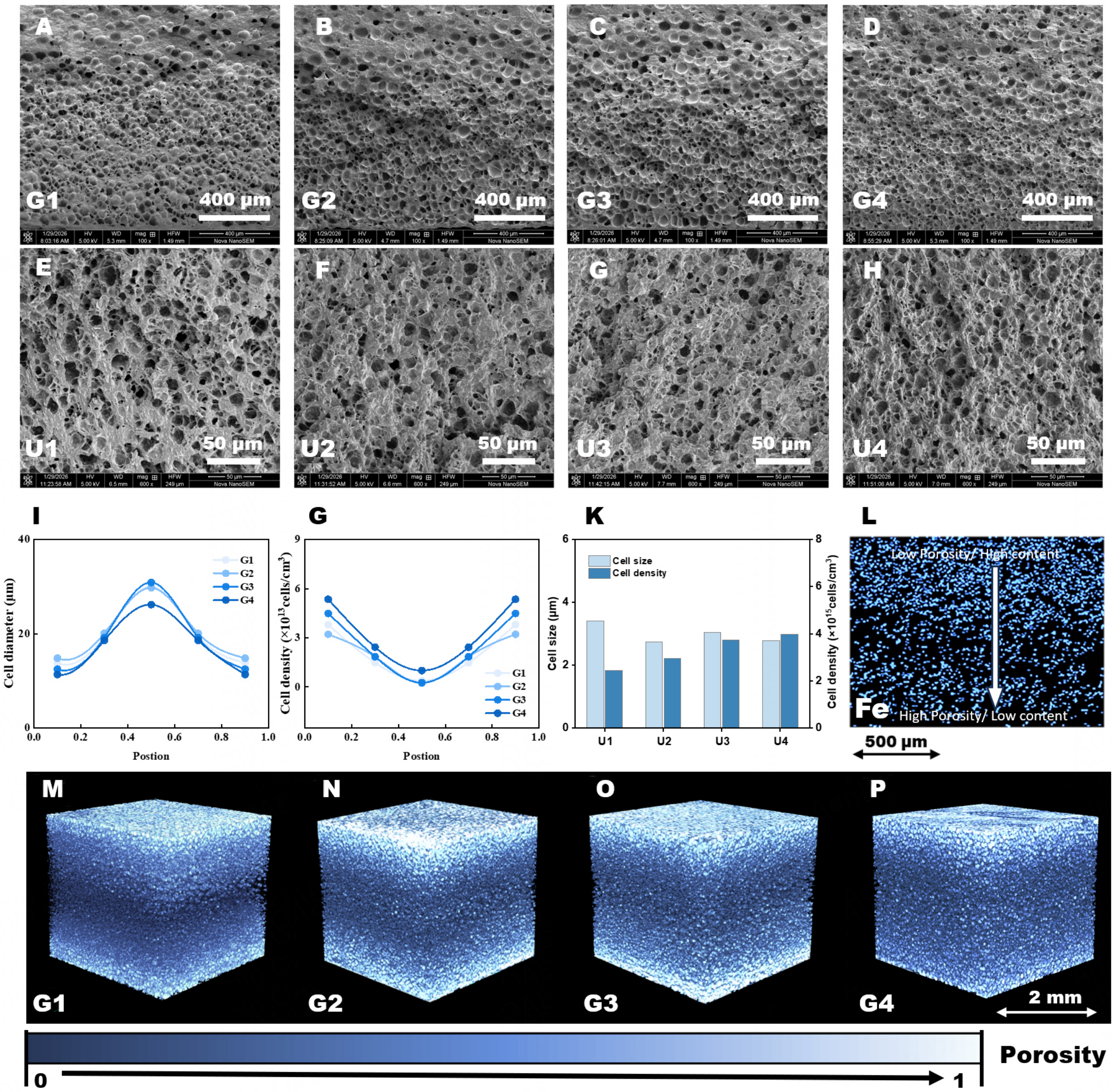

Figure 2. Characterization of microcellular structure morphology. SEM images of (A-D) G1-G4 and (E-H) U1-U4; (I) cell diameter and (J) cell density of gradient microcellular materials; (K) cell diameter and cell density of U1-U4; (L) EDS mapping of Fe elements in G2 and (M-P) Micro CT scan images of G1-G4.

To further assess the radar stealth capability of the materials, the radar cross-section (RCS) of a perfect electric conductor (PEC) plate, both pure PEC and coated with gradient microcellular FCIP/GP/SEBS materials at the optimal matching thickness, was simulated. As shown in Figure 4A-C and Supplementary Figure 6A-C, when EMW are incident perpendicularly, the RCS values of the PEC plate coated with gradient microcellular FCIP/GP/SEBS materials are significantly reduced compared to those of the pure PEC plate. Under perpendicular incidence, the RCS values of G1, G2, G3, and G4 are -20.19, -19.28, -19.11, and -19.70 dB·m^2, respectively, confirming excellent RCS reduction. Notably, at an incident angle of ±28°, sample G1 achieves a maximum RCS reduction of 35.77 dB·m^2, indicating strong suppression of EMW backscattering. Across an incident angle range of -89° to +89°, the maximum RCS curve of sample G1 remains below -20 dB·m^2, demonstrating outstanding radar stealth performance[39].

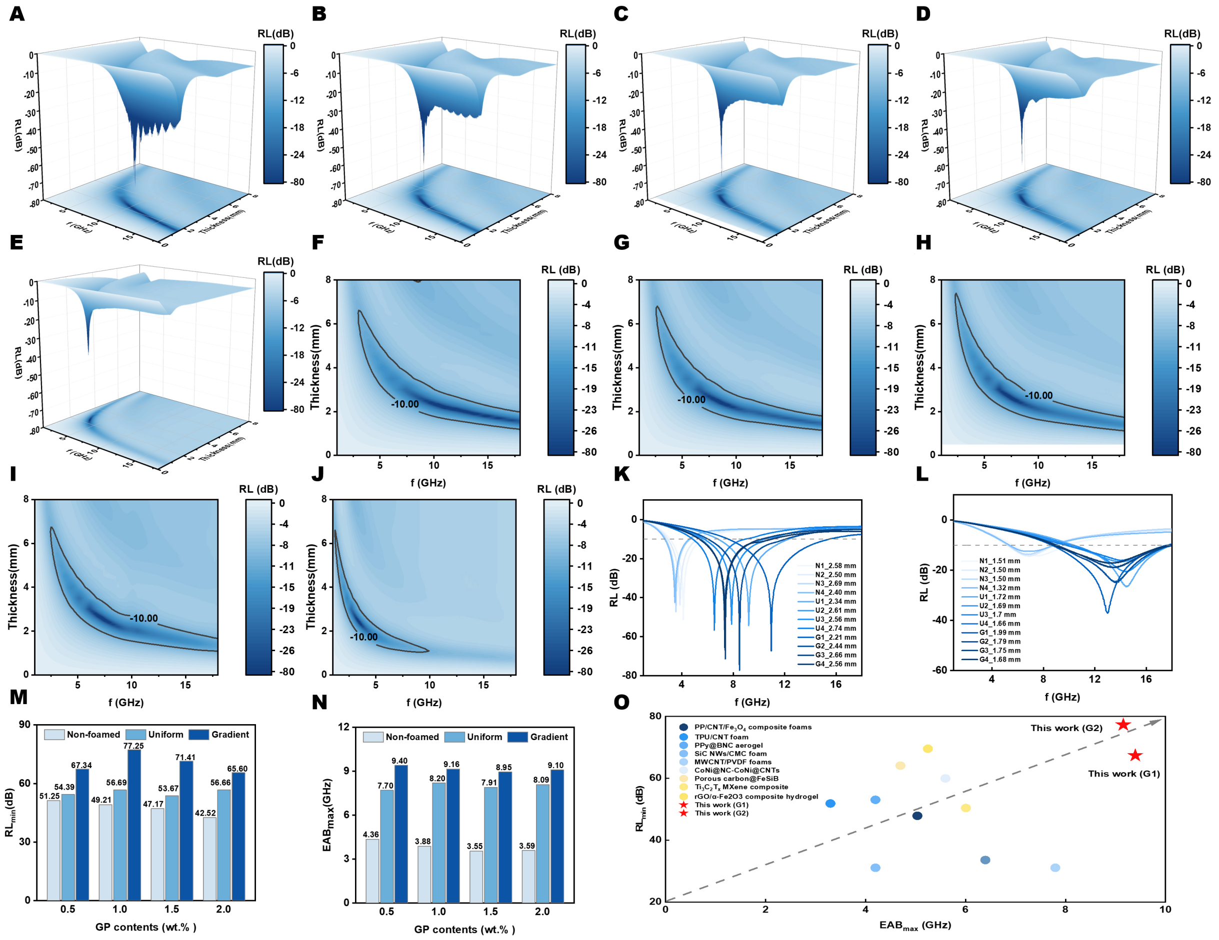

Figure 3. Microwave absorption properties. Electromagnetic wave absorption properties for G1, G2, G3, G4, and N4 depicted through (A-E) three-dimensional and (F-J) two-dimensional RL maps; (K) Minimum RL and corresponding thickness; (L) Maximum EAB and corresponding thickness; Histograms of (M) RL_{min} and (N) EAB_{max}, and (O) Comparison of RL_{min} and EAB_{max} with representative prior MA materials.

To evaluate the potential of these materials for practical military applications, we simulated the RCS curves of a pure PEC F-35 fighter model and coated with gradient microcellular FCIP/GP/SEBS materials, as shown in Figure 4D. To facilitate comparison of the optimal RCS stealth performance of different materials, we selected the optimal frequency and optimal thickness corresponding to the RL_{min} value of samples for simulation. At 10.96 and 8.48 GHz, the RCS curves under horizontal and vertical polarization were simulated at the nose aspect (θ = 90°, Φ = 0-360°) and the dorsal aspect (θ = 0-360°, Φ = 90°), respectively, for F-35 model coated with a 2.21 mm G1 layer [Figure 4E-H] and a 2.44 mm G2 layer [Supplementary Figure 6D-G]. Compared with the pure PEC fighter model, the RCS signals of the F-35 model coated with gradient microcellular MA material are significantly attenuated, confirming its superior radar stealth capability in military scenarios[40].

Electromagnetic parameters and microwave attenuation mechanism

Dielectric loss, magnetic loss, and impedance matching synergistically govern EMW absorption performance of materials[41,42]. The real part (ε′) and imaginary part (ε″) of the complex permittivity separately represent the storage and dissipation capacities for electric field energy, whereas the real part (μ′ and imaginary part μ″) of the complex permeability separately correspond to the storage and dissipation capacities of magnetic field energy[43].

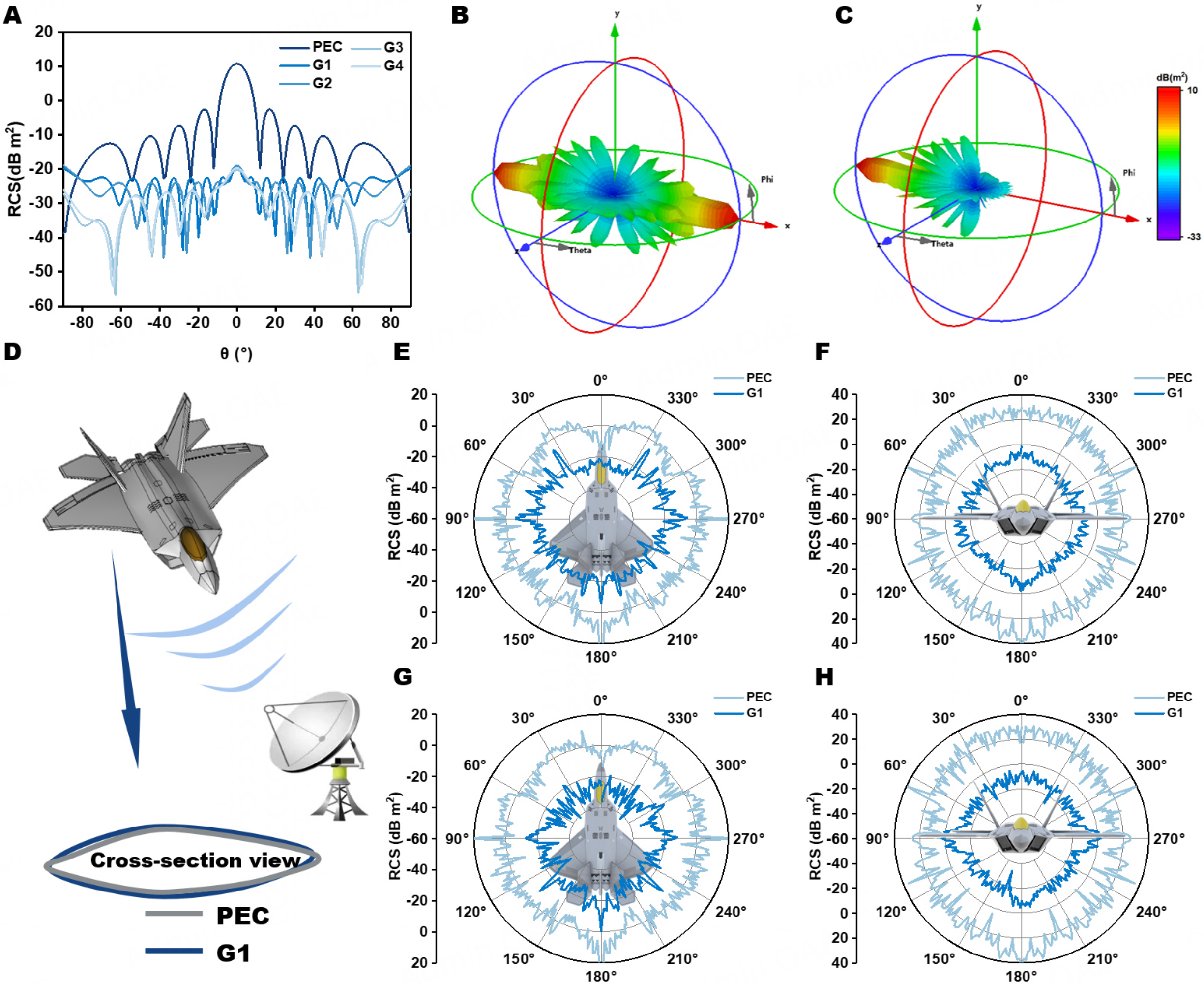

Figure 4. RCS Simulation Results. (A) Simulated RCS curves of the planar model from incident angles -89° to 89°; Simulated RCS plots of the planar model for (B) pure PEC and covered with (C) G1 at 10.96 GHz, (D) F-35 fighter model; Forward view RCS of the fighter aircraft covered with G1 at 10.96 GHz for (E) horizontal and (F) vertical polarization, respectively and top view RCS of the aircraft covered with G1 at 10.96 GHz for (G) horizontal and (H) vertical polarization, respectively.

As depicted in Supplementary Figure 7A and B, both ε′ and ε″ of the FCIP/GP/SEBS composites (N1-N4) gradually increase with increasing GP content. Distinct resonance peaks are observed in the ε′ and ε″ curves within specific frequency ranges, which are likely attributed to enhanced polarization relaxation induced by the heterogeneous interfaces among FCIP, GP, and the SEBS matrix. Notably, the ε′ and ε″ values of both the uniform and gradient microcellular FCIP/GP/SEBS materials are markedly lower than those of their unfoamed counterparts [Figure 5A, Supplementary Figure 7A and B], which primarily is attributed to the introduction of air (ε′ ≈ 1) by the microcellular structure. The significant downward trend appears especially after introducing gradient structure, mainly due to the lagging polarization behavior.

According to Debye theory[44], dielectric loss mainly arises from polarization loss and conduction loss, which are manifested as irregular semicircles and linear tails in the Cole-Cole plots[45], respectively. As illustrated in Supplementary Figure 8, the Cole-Cole plots of FCIP/GP/SEBS materials exhibit both semicircles and linear tails, indicating the coexistence of polarization relaxation dominated the dielectric loss owing to rich heterogeneous interfaces and conduction loss rising from conductive networks[46].

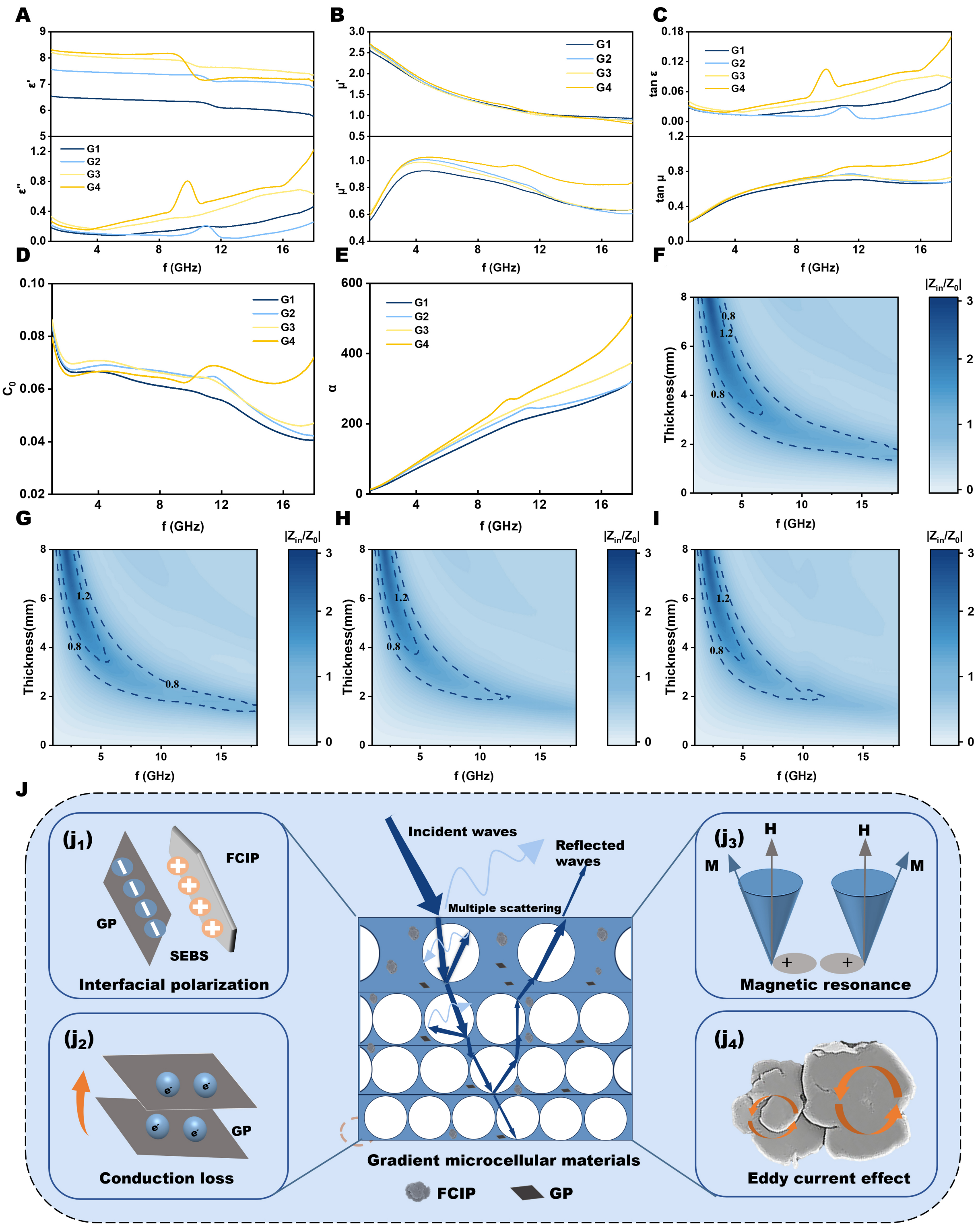

Figure 5. Electromagnetic Parameters and Microwave Attenuation Mechanism. (A) ε′ and ε″, (B) μ′ and μ″, (C) tan ε and tan μ, (D) C and (E) α plots of gradient microcellular FCIP/GP/SEBS materials; Impedance matching of (F) G1, (G) G2, (H) G3 and (I) G4; Multiple loss mechanisms of (J) integrated, (j_1-j_2) dielectric loss and (j_3-j_4) magnetic loss.

Figure 5B, Supplementary Figure 7C and D show that the μ′ and μ″ values of the FCIP/GP/SEBS materials vary within the ranges of 0.36-2.3 and 0.2-2.1, respectively. Compared with the unfoamed samples, the microcellular materials exhibit reduced μ′ and μ″ values. The pronounced fluctuation in μ″ are mainly ascribed to natural resonance at lower frequency and exchange resonance of FCIP under alternating electromagnetic field[47].

The dielectric loss tangent (tan ε = ε″/ε′) and magnetic loss tangent (tan μ = μ″/μ′) were used to evaluate the respective loss capacities. Figure 5C, Supplementary Figure 7E and F demonstrate that the samples have strong dielectric and magnetic loss capacities. The tan μ values are consistently higher than tan ε values, indicating that magnetic loss dominates the EMW attenuation process. This predominance arises from the natural resonance and magnetic dipole exchange resonance of abundant FCIP with high shape and magnetic anisotropy under alternating electromagnetic fields, contributing to the loss of microwave energy[48].

The magnetic loss includes natural resonance, exchange resonance, and eddy current loss[49], which is commonly characterized by the eddy current coefficient C_0 calculated from Equation (1):

$$C_0 = \mu''(\mu')^{-2}f^{-1} \tag{1}$$

Here, f is the EMW frequency.

As shown in Figure 5D, Supplementary Figure 7G, the relatively stable C_0 values of the microcellular FCIP/GP/SEBS materials suggest that eddy current loss is the primary magnetic loss mechanism, whereas samples N1-N4 exhibit pronounced exchange resonance at higher frequencies. Notably, the gradient microcellular samples show higher C_0 values than their uniform counterparts, which is attributed to the concentrated distribution of magnetic-dielectric fillers in the intermediate region of the gradient structure. This feature constructs a more effective electromagnetic coupling network, thereby promoting resonance loss through enhanced interactions among internal magnetic domains. Furthermore, with the increasing frequency, the electromagnetic mutual interaction within the electromagnetic coupling network constructed by FCIP and GP in the matrix further amplify magnetic resonance and eddy current effects[50]. Consequently, the synergistic interplay between dielectric and magnetic loss mechanisms plays a pivotal role in EMW dissipation[51].

Both impedance matching ($|Z_{in}/Z_0|$) and the attenuation constant (α) exert significant influences on EMW absorption performance. The α is calculated using Equation (2):

$$\alpha = \frac{\sqrt{2}\pi f}{c}\sqrt{(\mu''\varepsilon'' - \mu'\varepsilon') + \sqrt{(\mu''\varepsilon'' - \mu'\varepsilon')^2 + (\mu''\varepsilon'' + \mu'\varepsilon')^2}} \tag{2}$$

here, c is the speed of light.

As shown in Figure 5E and Supplementary Figure 7H, all samples exhibit high α values, indicating strong EMW dissipation and attenuation capabilities. Although samples N1-N4 possess higher α values, their severely mismatched impedance [Supplementary Figure 9A-D] hinders effective EMW absorption. Figure 5F-I, Supplementary Figure 9E-H show the $|Z_{in}/Z_0|$ values of the microcellular samples. Both the attenuation constant and the impedance matching area($|Z_{in}/Z_0|$ = 0.8-1.2) of the gradient microcellular samples are greater than those of their uniform counterparts, indicating enhanced EMW absorption and dissipation capabilities, which is consistent with the MA performance trend.

Owing to the gradient porosity and gradient microcellular structure, the effective electromagnetic parameters of the material vary gradually along the thickness direction, resulting in near-ideal impedance matching. The higher porosity in the surface region renders the equivalent characteristic impedance close to that of air (377 Ω), thereby facilitating EMW penetration into the material interior with minimal reflection. In contrast, the lower porosity in the interior region leads to a relatively concentrated distribution of electromagnetic fillers, consequently inducing stronger EMW attenuation. The gradient microcellular structure endows the samples with an excellent EMW attenuation system characterized by optimal surface impedance matching and strong internal EMWs attenuation. Even at relatively high GP contents, the gradient microcellular structure still endows the samples with the largest impedance-matching area.

Based on the above experimental results, the EMW absorption mechanisms of gradient microcellular FCIP/GP/SEBS materials were analyzed. In addition to gradient impedance matching, the contribution of the magnetic-dielectric loss filler system to EMW dissipation is also indispensable. On account of this gradient microcellular architecture, the dual magnetic-dielectric fillers FCIP and GP construct a highly efficient electromagnetic coupling network. The heterogeneous interfaces among FCIP, GP, and the matrix give rise to strong interfacial polarization, thereby enhancing polarization loss[52][Figure 5J_1]. The conductive network formed by multilayer GP facilitates electron hopping, thereby increasing conduction loss[42] [Figure 5J_2]. Owing to its high magnetic anisotropy, FCIP generates magnetic loss through natural resonance, exchange resonance, and eddy current effects under an alternating magnetic field[32] [Figure 5J_3 and J_4]. Meanwhile, the dense microcellular structure enables multiple reflections and scattering of EMW within the material, effectively prolonging the propagation path of EMWs [Figure 5J]. Therefore, the synergistic integration of the gradient microcellular structure and the coupled magnetic-dielectric filler networks effectively balance the attenuation constant and impedance matching of the material, thereby maximizing its EMW absorption performance. This unique and tunable gradient microcellular structural design provides an effective strategy for developing electromagnetic materials with broadband and high MA performance.

Multifunctional applications of gradient microcellular materials

Modern civilian and military applications impose stringent requirements on the multifunctionality of MA materials[31,53], including robust mechanical properties, water resistance, and energy-harvesting capability. To evaluate the mechanical properties of the materials, tensile tests were performed. Figure 6A summarizes the tensile strength and elongation at break of the different samples, with error bars representing the standard error from five independent measurements. The standard errors were 0.11, 0.15, 0.08, and 0.12 for tensile strength and 13.6, 13.4, 10.8, and 12.2 for elongation at break, respectively. The corresponding stress–strain curves are presented in Figure 6B. The favorable interfacial interactions between the GP filler and the SEBS matrix enable partial stress transfer and dispersion; however, excessive GP loading restricts the mobility of polymer chains and tends to induce stress concentration. Consequently, as the GP content increases from 0.5 to 2.0 wt.%, the elongation at break of samples N1-N4 progressively decreases from 400.6% to 244.1%, whereas the tensile strength correspondingly increases from 6.72 to 7.72 MPa. The microcellular structure of uniform or gradient microcellular materials can enhance energy dissipation and avoid sudden fracture caused by stress concentration, which may contribute to improving the elongation at break of the material[54,55]. Microcellular materials with a low expansion ratio of 2 possess smaller cell sizes and thicker cell walls, which may effectively mitigate the reduction in tensile strength typically induced by the microcellular structure[56]. Furthermore, compared with uniform microcellular counterparts relatively lower porosity within gradient microcellular materials provides stronger support, inhibiting crack propagation and local deformation.

In complex environments characterized by humidity, saline fog, or rainy conditions, the hydrophobicity of MA materials is critical to their long-term service reliability and stability. As illustrated in Figure 6C and Supplementary Figure 10, the FCIP/GP/SEBS composites undergo a remarkable transition from hydrophilicity to hydrophobicity after foaming. The dense microcellular architecture constructed by

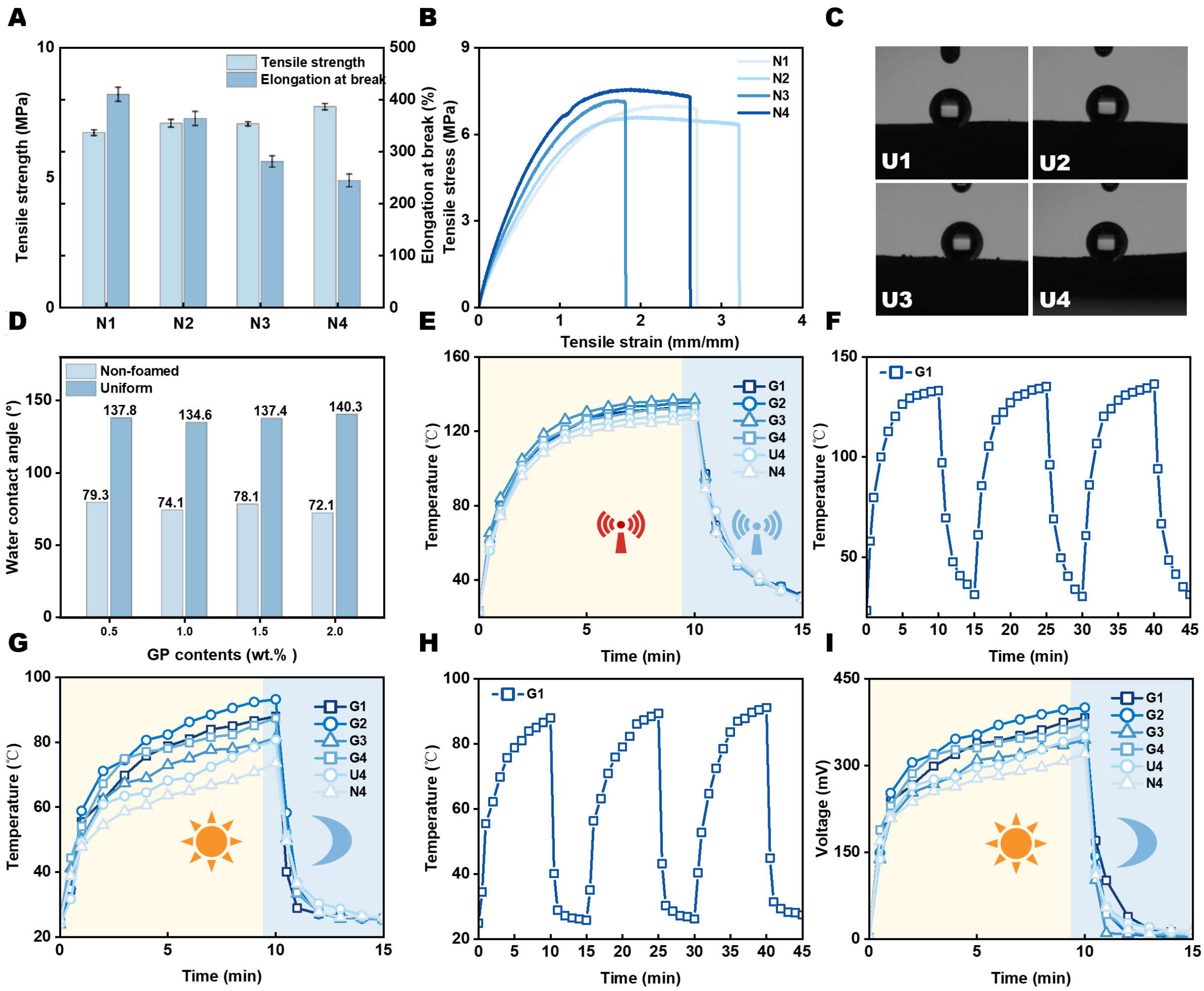

Figure 6. Multifunctional Applications of gradient microcellular materials. (A) Statistical bar chart of tensile strength and elongation at break of composites (error bars representing the standard error from five independent measurements); (B) Tensile stress-strain curves; (C) Images of water contact angle; (D) Water contact angle of composites and their microcellular materials; (E) Temperature change curves during magnetic heating and cooling processes; (F) Cyclic temperature change curves of G1 under magnetic heating and cooling processes; (G) Temperature curves during light-induced heating and cooling processes; (H) Cyclic temperature curves of G1 during light-induced heating and cooling processes; (I) Open-circuit voltage curves during photo-thermal-electric conversion.

supercritical N_2 foaming induces capillary effects at the surface while increasing the surface roughness, thereby endowing the microcellular materials with excellent hydrophobicity and water resistance. As shown in Figure 6D the water contact angles of the foamed samples U1, U2, U3, and U4 reach 137.8°, 134.6°, 137.4°, and 140.0°, respectively. Such hydrophobicity imparts the materials with self-cleaning and moisture-resistant properties.

To evaluate the magnetothermal conversion effect, the samples were placed in an alternating magnetic field, and their surface temperatures were monitored. Supplementary Figure 11 show the infrared thermal images of G1, G2, G3, G4, U4, and N4 recorded after magnetic-field exposure for 0, 0.5, 1, 3, 5, and 10 min. As illustrated in Figure 6E, the temperatures increase rapidly with exposure time, demonstrating excellent magnetothermal conversion performance. After exposure to the magnetic field for 10 min, the maximum surface temperatures of G1, G2, G3, G4, U4, and N4 reach 133.1, 135.8, 137.0, 132.9, 129.5, and 127.3 °C, respectively. The magnetic and highly anisotropic FCIP serves as the primary component responsible for magnetic energy dissipation and conversion, whereas GP with relatively high electrical conductivity further enhances magnetothermal conversion through thermal conduction, conduction loss, and localized heating

[57,58]. Under an alternating magnetic field, the gradient microcellular sample exhibits the optimal magnetothermal conversion capability. This can be attributed to the porosity gradient and filler distribution gradient formed by the gradient microcellular structure, which optimize the synergy between magnetic energy conversion and heat transfer. The filler enrichment in the central region of the gradient generates stronger hysteresis and eddy current losses, which are then efficiently transferred to the sample surface. Meanwhile, the high-porosity surface region acts as an insulating layer that retards heat dissipation, thereby sustaining a higher surface temperature. The T-t curves obtained over three repeated measurements, as shown in Figure 6F, indicate good magnetothermal conversion stability and reversibility. Thus, the stable magnetothermal conversion capability of samples offers considerable potential for applications in intelligent stealth, medical hyperthermia, energy recovery, and electromagnetic pollution mitigation.

To investigate the photothermal conversion behavior, the surface temperatures of the gradient microcellular FCIP/GP/SEBS materials were measured under simulated solar irradiation. Figure 6G depicts the real-time surface temperature curves of G1, G2, G3, G4,U4, and N4. After 10 min of illumination, the maximum surface temperatures of G1, G2, G3, G4, U4, and N4 reach 88.0, 93.2, 83.3, 87.4, 80.7, and 73.6 °C, respectively, as illustrated in Supplementary Figure 12. The superior photothermal conversion performance can be mainly attributed to the synergistic interaction between FCIP and GP, as well as their dark gray appearance, which promotes the photothermal effect[59]. The color indicates low optical reflectance and strong light-harvesting capability. Under simulated solar irradiation, electrons in FCIP and GP absorb photon energy and transition from the ground state to the excited state; upon returning to the ground state, part of the absorbed energy is dissipated as heat, thereby giving rise to a photothermal effect[4,60]. In addition, the conjugated structure formed by π-electron overlap in GP gives rise to non-radiative relaxation processes, further improving photothermal conversion efficiency[61-63]. The microstructure significantly influences the photothermal conversion efficiency of materials. The unfoamed material N4 may exhibit strong reflection of incident light and rapid heat dissipation, which are unfavorable for temperature rise. The uniform microcellular material U4 shows good thermal insulation but is prone to localized heat accumulation. In contrast, the gradient microcellular material G4 features a high-porosity surface that promotes multiple reflections and scattering of incident light among the cells, prolonging the effective absorption path[64]. The low-porosity interior, with a high filler concentration, efficiently converts the incoming light into heat via the FCIP and GP fillers. Meanwhile, the high-porosity surface region acts as an air-insulated thermal barrier[65]. Therefore, the gradient microcellular materials exhibit the optimal photothermal conversion capability. As depicted in Figure 6H, sample G1 exhibits stable T-t curves over three illumination cycles, demonstrating excellent cyclic stability and reusability of the photothermal conversion performance. To realize thermal energy recovery and utilization, the samples were placed on a thermoelectric module, and the output voltage was monitored as a function of illumination time [Figure 6I]. After 10 min of illumination, the output voltages of G1, G2, G3, and G4 reach 382.49, 400.27, 344.50, and 371.89 mV, respectively. Therefore, MA materials with photothermal conversion capability can provide an additional route for energy utilization during the operation of military aircraft[53].

In summary, the multifunctional integration of the gradient microcellular FCIP/GP/SEBS materials endow them with excellent thermal management and multi-field responsiveness capability, broadening the application potential of MA materials in complex environments.

CONCLUSIONS

In summary, gradient microcellular FCIP/GP/SEBS materials with a gradient porosity and microcellular size were successfully fabricated *via* a supercritical N_2 foaming strategy by regulating the foaming condition and component regulation. The gradient microcellular structure effectively optimizes electromagnetic parameters and improves impedance matching. The gradient porosity along the thickness direction endows MA materials with a gradient of effective electromagnetic parameters, inducing gradient impedance matching. The incident EMW can efficiently penetrate into the material interior and be dissipated through the synergistic effects of interfacial polarization, conduction loss, magnetic resonance, and eddy-current loss arising from the magnetic-dielectric fillers. And multiple reflection and scattering in microcellular structure also facilitate EMW absorption. Finally, the gradient microcellular materials exhibit markedly superior MA performance compared with their unfoamed and uniform microcellular counterparts, with G1 achieving an RL of -67.34 dB at 2.21 mm and an EAB of 9.40 GHz at 1.99 mm, nearly covering the entire X and Ku bands. The beneficial roles of the gradient microcellular structure in optimizing impedance matching and RCS reduction were further confirmed by electromagnetic simulation. In addition, the integrated multifunctionality of favorable mechanical performance, excellent hydrophobicity, and stable photothermal and magnetothermal conversion broadens the application prospects of the gradient microcellular FCIP/GP/SEBS materials in radar stealth, thermal management, and electromagnetic pollution control.

DECLARATIONS

Authors' contributions

Fabrication and testing of materials, data collection, software simulation and original manuscript writing: Wang, X.; Chen, Y.

Validation and original manuscript revision: Chen, Y.; Hu, D.; Zhao, L.

Investigation, data curation, formal analysis and chart design: Lei, K.; Li, X.; Sun, J.

Resources, project administration, funding acquisition: Chen, Y.; Zhao, L.

Availability of data and materials

The raw data supporting the findings of this study are available within this Article and its Supplementary Materials. Further data is available from the corresponding authors upon reasonable request.

AI and AI-assisted tools statement

Not applicable.

Financial support and sponsorship

This work was supported by the National Natural Science Foundation of China (grant no. 22308097), the Shanghai Post-doctoral Excellence Program (grant no. 2022765), the Program of China Scholarship Council (grant no. 202406740023), the Young Elite Scientists Sponsorship Program by CAST (grant no. 2024QNRC001) and the Fundamental and Interdisciplinary Disciplines Breakthrough Plan of the Ministry of Education of China (grant no. JYB2025XDXM407).

Conflicts of interest

All authors declared that there are no conflicts of interest.

Ethical approval and consent to participate

Not applicable.

Consent for publication

Not applicable.

Copyright

Supplementary Materials

Supplementary Materials

REFERENCES

1. Wang, L.; Cai, Z.; Su, L.; et al. Bifunctional SiC/Si_3N_4 aerogel for highly efficient electromagnetic wave absorption and thermal insulation. *J. Adv. Ceram.* **2023**, *12*, 309-20. DOI

2. Yan, Y.; Zhang, K.; Qin, G.; et al. Phase engineering on MoS_2 to realize dielectric gene engineering for enhancing microwave absorbing performance. *Adv. Funct. Mater.* **2024**, *34*, 2316338. DOI
3. Zong, J.; Zhou, X.; Hu, Y.; et al. A wearable multifunctional fabric with excellent electromagnetic interference shielding and passive radiation heating performance. *Compos. B. Eng.* **2021**, *225*, 109299. DOI
4. Zhu, L.; Tian, L.; Jiang, S.; et al. Advances in photothermal regulation strategies: from efficient solar heating to daytime passive cooling. *Chem. Soc. Rev.* **2023**, *52*, 7389-460. DOI
5. Lv, H.; Yang, Z.; Pan, H.; Wu, R. Electromagnetic absorption materials: current progress and new frontiers. *Prog. Mater. Sci.* **2022**, *127*, 100946. DOI
6. Xiang, J.; Zhang, Y.; Liu, X.; et al. Natural polyphenols-platinum nanocomplexes stimulate immune system for combination cancer therapy. *Nano. Lett.* **2022**, *22*, 5615-25. DOI
7. Li, N.; Zong, Z.; Li, Z. Y.; et al. Dual-gradient structure design in polyimide foam for efficient and ultra-broadband microwave absorption. *Small* **2025**, *21*, e10100. DOI
8. Xu, Y.; Yang, Y.; Yan, D.; Duan, H.; Zhao, G.; Liu, Y. Gradient structure design of flexible waterborne polyurethane conductive films for ultraefficient electromagnetic shielding with low reflection characteristic. *ACS. Appl. Mater. Interfaces.* **2018**, *10*, 19143-52. DOI
9. Wang, X.; Chen, X.; He, Q.; et al. Bidirectional, multilayer MXene/polyimide aerogels for ultra-broadband microwave absorption. *Adv. Mater.* **2024**, *36*, 2401733. DOI
10. Xue, T.; Yang, Y.; Yu, D.; et al. 3D printed integrated gradient-conductive MXene/CNT/Polyimide aerogel frames for electromagnetic interference shielding with ultra-low reflection. *Nano. Micro. Lett.* **2023**, *15*, 45. DOI PubMed PMC
11. Ma, W.; Liu, X.; Yang, T.; et al. Strong magnetic-dielectric synergistic gradient metamaterials for boosting superior multispectral ultra-broadband absorption with low-frequency compatibility. *Adv. Funct. Mater.* **2024**, *35*, 2314046. DOI
12. Ma, Z.; He, J.; Liu, S.; et al. Gradient layered MXene/Fe_3O_4@CNTs/TOCNF ultrathin nanocomposite paper exhibiting effective electromagnetic shielding and multifunctionality. *Nano. Res.* **2024**, *17*, 8233-42. DOI
13. Xue, B.; Li, Y.; Cheng, Z.; et al. Directional electromagnetic interference shielding based on step-wise asymmetric conductive networks. *Nano-Micro. Lett.* **2021**, *14*, 16. DOI PubMed PMC
14. Qu, N.; Sun, H.; Sun, Y.; et al. 2D/2D coupled MOF/Fe composite metamaterials enable robust ultra-broadband microwave absorption. *Nat. Commun.* **2024**, *15*, 5642. DOI PubMed PMC
15. Jiang, C.; Wang, Y.; Zhao, Z.; Ma, Z.; Liu, Y. Multifunctional three-dimensional porous MOFs derived Fe/C/carbon foam for microwave absorption, thermal insulation and infrared stealth. *Ceram. Int.* **2023**, *49*, 18861-9. DOI
16. Wang, S.; Huang, X.; Zhang, W. Preparation of graphene/flaky carbonyl iron/polyurethane foam composites and research on their microwave absorption properties. *Appl. Phys. A.* **2021**, *127*, 742. DOI
17. Cheng, H.; Pan, Y.; Wang, X.; et al. Ni Flower/MXene-melamine foam derived 3D magnetic/conductive networks for ultra-efficient microwave absorption and infrared stealth. *Nano. Micro. Lett.* **2022**, *14*, 63. DOI PubMed PMC
18. Jia, X.; Zhong, W.; Chen, Y.; et al. Density gradient structure foams prepared by novel two-step foaming strategy: performance, simulation and optimization. *Compos. B. Eng.* **2025**, *288*, 111890. DOI
19. Wang, G.; Liu, J.; Zhao, J.; Li, S.; Zhao, G.; Park, C. B. Structure-gradient thermoplastic polyurethane foams with enhanced resilience derived by microcellular foaming. *J. Supercrit. Fluids.* **2022**, *188*, 105667. DOI
20. Zhou, Q.; Shi, T.; Xue, B.; et al. Gradient carbonyl-iron/carbon-fiber reinforced composite metamaterial for ultra-broadband electromagnetic wave absorption by multi-scale integrated design. *Int. J. Miner. Metall. Mater.* **2023**, *30*, 1198-206. DOI
21. Yang, J.; Liao, X.; Wang, G.; et al. Heterogeneous silicon rubber composite foam with gradient porous structure for highly absorbed ultra-efficient electromagnetic interference shielding. *Compos. Sci. Technol.* **2021**, *206*, 108663. DOI
22. Luo, F.; Liu, D.; Cao, T.; et al. Study on broadband microwave absorbing performance of gradient porous structure. *Adv. Compos. Hybrid. Mater.* **2021**, *4*, 591-601. DOI
23. Zhang, Y.; Pan, L.; Zhang, P.; Sun, Z. Gradient multilayer design of $Ti_3C_2T_x$ MXene nanocomposite for strong and broadband microwave absorption. *Small. Sci.* **2022**, *2*, 2200018. DOI PubMed PMC
24. Monnereau, L.; Urbanczyk, L.; Thomassin, J.; et al. Gradient foaming of polycarbonate/carbon nanotube based nanocomposites with supercritical carbon dioxide and their EMI shielding performances. *Polymer* **2015**, *59*, 117-23. DOI
25. Mosanenzadeh S, Naguib HE, Park CB, Atalla N. Design and development of novel bio-based functionally graded foams for enhanced acoustic capabilities. *J. Mater. Sci.* **2014**, *50*, 1248-56. DOI
26. Zhu, L.; Wang, G.; Xu, Z.; Li, X.; Yang, C.; Zhao, G. A new microcellular foaming strategy to develop structure-gradient thermoplastic polyurethane foams with enhanced elasticity. *Mater. Des.* **2023**, *234*, 112325. DOI
27. Naebe, M.; Shirvanimoghaddam, K. Functionally graded materials: a review of fabrication and properties. *Appl. Mater. Today.* **2016**, *5*, 223-45. DOI

28. Ren, X.; Wang, J.; Wang, T.; Li, Z.; Han, S.; Sun, G. Fabrication of one-step shape memory gradient sound absorber with wrinkled inner wall and closed-pore structure. *Eur. Polym. J.* **2023**, *196*, 112226. DOI
29. Martins, P.; Lanceros-Mendez, S. Chapter Eleven - Magnetic field into multifunctional materials: magnetorheological, magnetostrictive, and magnetocaloric. In: Advanced lightweight multifunctional materials. Woodhead Publishing; 2021, pp. 391-405. DOI
30. Zhang, K.; Zhang, J.; Hou, Z.; Bi, S.; Zhao, Q. Multifunctional broadband microwave absorption of flexible graphene composites. *Carbon* **2019**, *141*, 608-17. DOI
31. Xiao, J.; He, M.; Zhan, B.; et al. Multifunctional microwave absorption materials: construction strategies and functional applications. *Mater. Horiz.* **2024**, *11*, 5874-94. DOI
32. Zhang, K.; Wang, Z.; Yan, Y.; et al. Dielectric-magnetic manipulation of reduced graphene oxide permittivity for enhanced electromagnetic wave absorption. *J. Adv. Ceram.* **2024**, *13*, 1974-84. DOI
33. Wu, L.; Wang, G.; Shi, S.; et al. Ni-carbon microtube/polytetrafluoroethylene as flexible electrothermal microwave absorbers. *Adv. Sci.* **2023**, *10*, 2304218. DOI PubMed PMC
34. Dong, M.; Wang, G.; Zhang, X.; et al. An overview of polymer foaming assisted by supercritical fluid. *Adv. Compos. Hybrid. Mater.* **2023**, *6*, 207. DOI
35. He, Z.; Shi, L.; Sun, R.; et al. Low-temperature oxidation induced phase evolution with gradient magnetic heterointerfaces for superior electromagnetic wave absorption. *Nano. Micro. Lett.* **2024**, *17*, 7. DOI PubMed PMC
36. Wei, Z.; Li, Z.; Chen, D.; Liang, J.; Kong, J. Recent progress of advanced composites for broadband electromagnetic wave absorption. *Small. Struct.* **2024**, *6*, 2400615. DOI
37. Xu, H.; Zhan, H.; Xu, Z.; et al. Sandwich-like CNTs/Carbon@Si_3N_4 porous foam for temperature-insensitive electromagnetic wave absorption. *Adv. Funct. Mater.* **2025**, *35*, 2421242. DOI
38. Zhong, X.; He, M.; Zhang, C.; Guo, Y.; Hu, J.; Gu, J. Heterostructured BN@Co-C@C endowing polyester composites excellent thermal conductivity and microwave absorption at C band. *Adv. Funct. Mater.* **2024**, *34*, 2313544. DOI
39. Xie, K.; Zhang, Q.; Chen, F.; Fu, Q. Largely enhanced electromagnetic wave absorption*via* surface coating of carbonyl iron particles with liquid metal. *J. Mater. Chem. A.* **2025**, *13*, 1887-96. DOI
40. Han, Y.; Chen, F.; Fu, Q. Heterogeneous three-dimensional FeSiAl@SiO_2@MoS_2 composite with a SiO_2 wave-transmitting layer for enhanced electromagnetic wave absorption performance. *J. Mater. Chem. A.* **2024**, *12*, 25322-33. DOI
41. Mao, H.; Zhong, X.; Liu, X.; et al. Study on electrical conductivity and microwave absorption properties of CNTs/CB/PMMA nanocomposites foam. *Mater. Res. Express.* **2021**, *8*, 126301. DOI
42. Xiao, J.; Zhan, B.; He, M.; et al. Interfacial polarization loss improvement induced by the hollow engineering of necklace-like PAN/carbon nanofibers for boosted microwave absorption. *Adv. Funct. Mater.* **2024**, *35*, 2316722. DOI
43. Liang, H.; Chen, G.; Liu, D.; et al. Exploring the Ni 3*d* orbital unpaired electrons induced polarization loss based on Ni single-atoms model absorber. *Adv. Funct. Mater.* **2022**, *33*, 2212604. DOI
44. Gao, T.; Zhao, R.; Li, Y.; et al. Sub-nanometer Fe clusters confined in carbon nanocages for boosting dielectric polarization and broadband electromagnetic wave absorption. *Adv. Funct. Mater.* **2022**, *32*, 2204370. DOI
45. Li, Z.; Zhang, L.; Wu, H. A regulable polyporous graphite/melamine foam for heat conduction, sound absorption and electromagnetic wave absorption. *Small* **2023**, *20*, 2305120. DOI
46. Xia, Y.; Gao, W.; Gao, C. A review on graphene-based electromagnetic functional materials: electromagnetic wave shielding and absorption. *Adv. Funct. Mater.* **2022**, *32*, 2204591. DOI
47. Wang, S.; Zhang, X.; Hao, S.; et al. Nitrogen-doped magnetic-dielectric-carbon aerogel for high-efficiency electromagnetic wave absorption. *Nano-Micro. Lett.* **2023**, *16*, 16. DOI PubMed PMC
48. Zou, Z.; Ning, M.; Lei, Z.; et al. 0D/1D/2D architectural Co@C/MXene composite for boosting microwave attenuation performance in 2-18 GHz. *Carbon* **2022**, *193*, 182-94. DOI
49. Liu, P.; Li, Y.; Xu, H.; et al. Hierarchical Fe-Co@TiO_2 with incoherent heterointerfaces and gradient magnetic domains for electromagnetic wave absorption. *ACS. Nano.* **2023**, *18*, 560-70. DOI
50. Shi, X.; You, W.; Li, X.; Wang, L.; Shao, Z.; Che, R. In-situ regrowth constructed magnetic coupling 1D/2D Fe assembly as broadband and high-efficient microwave absorber. *Chem. Eng. J.* **2021**, *415*, 128951. DOI
51. Pan, F.; Rao, Y.; Batalu, D.; et al. Macroscopic electromagnetic cooperative network-enhanced MXene/Ni chains aerogel-based microwave absorber with ultra-low matching thickness. *Nano. Micro. Lett.* **2022**, *14*, 140. DOI PubMed PMC
52. Qin, M.; Zhang, L.; Wu, H. Dielectric loss mechanism in electromagnetic wave absorbing materials. *Adv. Sci.* **2022**, *9*, 2105553. DOI PubMed PMC
53. Yao, L.; Wang, Y.; Zhao, J.; Zhu, Y.; Cao, M. Multifunctional nanocrystalline-assembled porous hierarchical material and device for integrating microwave absorption, electromagnetic interference shielding, and energy storage. *Small* **2023**, *19*, 2208101. DOI

54. Zhong, W.; Chen, Y.; Sun, J.; Wang, X.; Hu, D.; Zhao, L. Preparation of SEBS foam for new-generation sports protection and monitoring by microwave selective sintering. *Chem. Eng. J.* **2025**, *515*, 163494. DOI
55. Ghahramani, P.; Behdinan, K.; Moradi-Dastjerdi, R.; Naguib, H. E. Development and modeling of an ultra-robust TPU-MWCNT foam with high flexibility and compressibility. *Nanotechnol. Rev.* **2024**, *13*, 20230219. DOI
56. Kıroğlu, C.; Kızılcan, N. Production and characterization of thermoplastic elastomer foams based on the styrene-ethylene-butylene-styrene (SEBS) rubber and thermoplastic material. *Open. Chem.* **2021**, *19*, 929-37. DOI
57. Zhang, F.; Miao, X.; Van Dijk, N.; Brück, E.; Ren, Y. Advanced magnetocaloric materials for energy conversion: recent progress, opportunities, and perspective. *Adv. Energy. Mater.* **2024**, *14*, 2400369. DOI
58. Zhang, S.; Li, W.; Wu, H.; Jiao, J. Multi-optimized flexible graphene oxide/multi-walled carbon nanotubes/ferroferric oxide nanopaper with enhanced electromagnetic wave absorption performance. *Adv. Compos. Hybrid. Mater.* **2023**, *6*, 154. DOI
59. Liu, G.; Xu, J.; Wang, K. Solar water evaporation by black photothermal sheets. *Nano. Energy.* **2017**, *41*, 269-84. DOI
60. Yun, J. Recent progress in thermal management for flexible/wearable devices. *Soft. Sci.* **2023**, *3*, 12. DOI
61. Yang, Y.; Shao, L.; Wang, J.; Ji, Z.; Su, C.; Li, C. Flexible Janus-structured composite films for low-reflection EMI shielding, photothermal conversion, and infrared stealth. *J. Mater. Sci. Technol.* **2026**, *271*, 236-46. DOI
62. Hu, F.; Li, M.; Li, P.; et al. High-performance multifunctional nanopapers with superior mechanical strength, electromagnetic interference shielding, and thermal management for next-generation electronics. *Adv. Funct. Mater.* **2024**, *35*, 2418899. DOI
63. Liu, C.; Chen, G.; Zhang, Z.; You, Y. Expanding the conjugate structure of polymeric carbon nitride for enhanced light absorption and photothermal conversion. *Macromol. Rapid. Commun.* **2021**, *42*, 2100502. DOI
64. Shi, Y.; Wang, Y.; Meng, N.; Liao, Y. Photothermal conversion porous organic polymers: design, synthesis, and applications. *Small. Methods.* **2024**, *8*, 2301554. DOI
65. Fu, R.; Cao, X.; Zhang, H.; et al. High-efficient solar steam generation assisted removal of radioactive iodine ions from water by carbonized conjugated microporous polymer-based photothermal conversion materials. *Sep. Purif. Technol.* **2024**, *330*, 125283. DOI